AIAA SCITECH 2024 Forum, 8-12 January 2024, Orlando, USA
DOI:10.2514/6.2024-2501

Motion Estimation of an Aircraft Model Using Computer Vision

Pavithra Kasula*, James F. Whidborne.†, Zeeshan Rana‡ and Ademayowa Ishola§
School of Aerospace, Transport and Manufacturing, Cranfield University, United Kingdom

Dynamic wind tunnel tests are used to investigate the flight dynamics of aircraft. Currently contact measurement systems are used which increase friction and require on-board instrumentation. A vision-based method is proposed in this paper. The method uses a sequential process of Harris corner detection, Kanade-Lucas-Tomasi tracking, and Euler angles to identify the Euler angles from a pair of cameras, one with a top-view and the other with a side-view. The method is tested by simulating a 3D CAD model for a single degree of freedom rotational motion. The results have been quantified through numerical analysis and the proposed method is analysed analytically. The developed method is effective when integrated with another method of instrumentation such as an IMU.

I. NOMENCLATURE

F	=	2D grey-scale image
u	=	pixel coordinate in the x direction
v	=	pixel coordinate in the y direction
c_x	=	principal point in the x direction
c_y	=	principal point in the y direction
X_I	=	image coordinates in the x direction
Y_I	=	image coordinates in the y direction
X_C	=	camera coordinates in the x direction
Y_C	=	camera coordinates in the y direction
Z_C	=	camera coordinates in the z direction
f	=	focal length
X	=	3D coordinates in the x direction
Y	=	3D coordinates in the y direction
Z	=	3D coordinates in the z direction
R_T	=	rotation matrix of body coordinates to camera coordinates for top view
R_S	=	rotation matrix of body coordinates to camera coordinates for side view
R_R	=	rotation matrix of body coordinates to camera coordinates of relative pose
t_T	=	top view translation vector of body coordinates to camera coordinates
t_S	=	side view translation vector of body coordinates to camera coordinates
t_R	=	relative pose translation vector of body coordinates to camera coordinates
R	=	Euler angle rotation matrix
ϕ	=	roll angle
θ	=	pitch angle
ψ	=	yaw angle
$\dot{\phi}$	=	Euler roll rate
$\dot{\theta}$	=	Euler pitch rate
$\dot{\psi}$	=	Euler yaw rate

*PhD Researcher, Cranfield University.
†Professor of Control Engineering, Cranfield University.
‡Senior Lecturer in Aerodynamics, Cranfield University.
§PhD Researcher, Cranfield University.

II. INTRODUCTION

For the design of new aircraft, flight dynamics models are required for the assessment of handling qualities, design of the flight control system and for flight simulation. This should be done at the early design stages. In addition, subscale flight demonstrators can be built which provide an early assessment of the design, validate the model and enables the development process of the model [1]. To parameterize the model, identification of the model parameters is needed. Approaches to flight dynamics identification include theoretical and numerical analysis, wind tunnel testing and flight testing. In the early stage of design, parameters are estimated theoretically which have limited accuracy, and so wind tunnel testing is required. Subscale models can also be placed into a wind tunnel to extract the aerodynamic and flight dynamics data.

Static wind tunnel testing is usually used to identify the main parameters such as lift and drag. However non-linear flight regimes involving high angles of attack require investigation of non-steady aerodynamics, and dynamic wind tunnel (DWT) testing can enable this [2]. Although dynamic wind tunnel testing is not widely used, modern methods of model building (3D printing) and advances in instrumentation are making dynamic wind tunnel experiments more accessible and affordable for inclusion in the design process.

Various DWT testing techniques have been developed to determine the forces acting on the model such as captive (forced oscillation and rotary balance) test, single-degree-of-freedom (free-to-pitch or free-to-yaw and free-to-roll) test and free-flying test. A captive test is used to measure damping and rotary derivatives and is driven by a support mechanism that does not enable a free motion similar to a real flight. The single-degree-of-freedom test are used to measure dynamic stability derivatives, free-motion modes, and assess unsteady aerodynamics effects on the model's motion. The model has a free motion with a support apparatus with an initial condition. The two categories of the free-flying test are the low speed with power system and high speed without power system [3] [4].

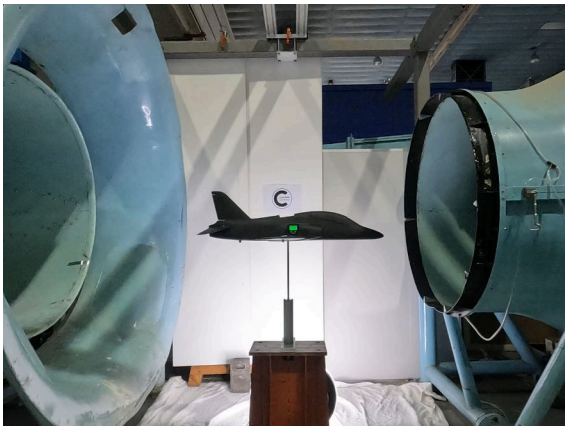

Fig. 1 3-DOF Aircraft model in DWT.

The widely preferred option for a free flying testing rig is a 3-DOF rotational motion rig as this allows for measurement of forces via a balance located either at the rig mount or at the model's attachment point. The DWT testing rig available at Cranfield University is an open section tunnel with 1.5×1.1m working section and maximum speed of 40m/s that allows investigating of 4-DOF (roll, pitch, yaw and heave) of motion. The range of roll and pitch motion is $\pm 30^\circ$, range of yaw motion is 360° and the maximum range of heave translation motion is 0.75m [5]. The figures 1 and 2 shows the Cranfield University's DWT rig with $1/12$ size of the BAe Hawk model that allows 3-DOF with a bottom rig mount and 4-DOF of motion with the model suspended on a stiff vertical rod respectively. The DWT testing rig at University of Bristol has a maximum 5-DOF by having a 2-DOF gimbal at the pendulum attachment and a 3-DOF gimbal mounted at the model centre of gravity [6] [7] [8].

Instrumentation can be placed on-board the aircraft model and are widely used. Inertial Measurement Unit (IMU) are non-contact but measure rotation rates and displacement accelerations. Angles can be measured on-board using potentiometers on the gimbal. However, non-contact methods such as cameras are not extensively used for measurements of aerodynamic data. An IMU consists of three gyroscopes and three accelerometers mounted in a set of three orthogonal axes which measures the rotation rate and acceleration in all three dimensions. The bias performances of micro-electro-mechanical systems (MEMS) and ring laser gyro (RLG) based IMUs from Honeywell, range from 0.25 deg/hr to 7 deg/hr and 0.25 deg/hr to 0.0006 deg/hr [9]. The IMUs with less bias are expensive and are not yet

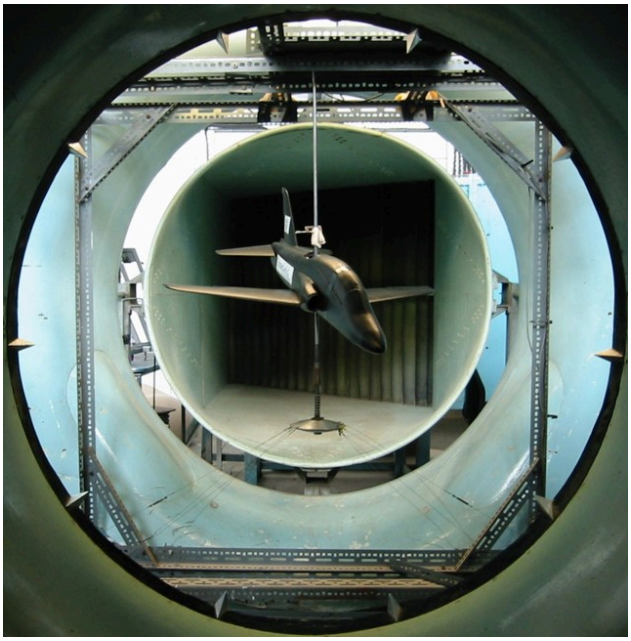

Fig. 2 4-DOF Aircraft model in DWT.

compact enough for most DWT testing models. A low-cost and smaller IMU (MEMS) sensors can be used for testing of scaled models. Although these sensors have their merits, they do not achieve the same level of accuracy as the others. This accuracy reduction in unit is caused due to errors, namely bias error, repeatability, stability, drift, sensor noise, misalignment, and latency. Sensor fusion (Global Positioning System, multiple IMUs, vision system) and model-based techniques (extended Kalman filter, Sage-Husa adaptive Kalman filter [10]) are widely known approaches to reduce the errors in the measurement unit [11]. Deep neural networks are gaining interest in learning systematic drift errors [12] by formulating the problem as optimisation instead of traditional integration.

High-speed cameras are versatile off-board sensors able to provide real-time data. Implementing vision systems in wind tunnel testing can be an advantage for flight dynamic models identification. However, their performance is affected by inadequate light settings and precise background settings amongst other factors. Object detection techniques using laser and self luminous markers [13], multiple line marks on side of train model [14], markers [15] have been used for pose measurements in wind tunnels. Object tracking techniques based on particle filtering [16], saliency combined particle filtering [17], and background subtraction [18] have been used for aerial UAV tracking. The wide range of advances in computer vision techniques gives an opportunity to improve the accuracy of the data acquired in dynamic wind tunnel experiments.

Camera pose estimation and triangulation are fundamental problems in computer vision that involve determining the position and orientation of a camera and reconstructing the 3D structure of a scene. The Direct Linear Transform (DLT) method and the Perspective-n-Point (PnP) algorithm are commonly employed techniques for solving these problems. The DLT method [19] focuses on 3D triangulation. It estimates the camera projection matrix based on 2D-3D correspondences, allowing for the reconstruction of the complete 3D scene. However, the DLT method has limitations, including sensitivity to noise, lack of robustness to outliers, difficulties with planar scenes, and the assumption of known camera intrinsics.

In contrast, the PnP algorithm, popularized by [20], specifically addresses camera pose estimation from 2D-3D correspondences. It aims to determine the camera's position and orientation by leveraging the geometric constraints between the 3D points and their corresponding 2D projections. While the PnP algorithm has gained significant attention and is widely cited, it also has limitations. These include sensitivity to noise, the requirement of a minimum number of correspondences, and the potential for ambiguous solutions. To address the limitations of these methods, various extensions and improvements have been proposed. For example, the EPnP algorithm by [21] offers an efficient solution for PnP pose estimation. These methods serve as valuable tools for camera pose estimation and triangulation. However, researchers continue to explore novel techniques and advancements to enhance the accuracy, robustness, and efficiency of these approaches in real-world applications.

Computer vision-based estimation of aircraft dynamics has been researched by [22] from optical flow observed by a downward looking camera, solved by extended Kalman Filter and analysed by Monte Carlo simulations. Whereas the research presented in this paper utilizes 3D CAD simulations that enable real-world conditions and environments to be applied to reproduce real-world experiments. This helps in identifying errors and the setting of multiple degrees of freedom for a model. MATLAB Simscape enables modelling, simulation and visualisation of the CAD model. Although [22] use Monte Carlo simulations, these focus on statistical analysis and uncertainty assessment, whereas Simscape simulations focus on the dynamic behaviour and performance analysis of physical systems. They are used to simulate and analyze the time-domain response, transient behaviour, steady-state characteristics, and control of physical systems. Simscape is particularly useful for designing and testing control systems and evaluating system performance under various conditions. This method of testing compared to [22] before conducting a dynamic wind tunnel testing is cost effective and comparable to the real-world experimental results.

In this paper, a novel method is proposed to obtain accurate dynamic wind tunnel data of a scaled rigid body aircraft model without markers. The method uses a sequential process of Harris corner detection, Kanade-Lucas-Tomasi tracking, and Euler angles to estimate the motion of the aircraft model. This method is validated by simulating, in MATLAB Simscape, a 3D CAD model of a 1/12 sub-scale model of the BAe Hawk fighter aircraft.

The rest of this paper is structured as follows. Section III discusses the motion estimation using our proposed method, Section III.G details the 3D CAD model simulation, Section III.H discusses the conducted sensitivity analysis, and Section IV discusses the results. Conclusions are given in the final section.

III. MOTION ESTIMATION

The proposed method estimates the attitude of the object. The following assumptions are considered, the model is a rigid body, has a single fixed centre of rotation. To increase the applicability of the research, motion estimation without using visual markers on the model is implemented. Figure 3 depicts the process of the method.

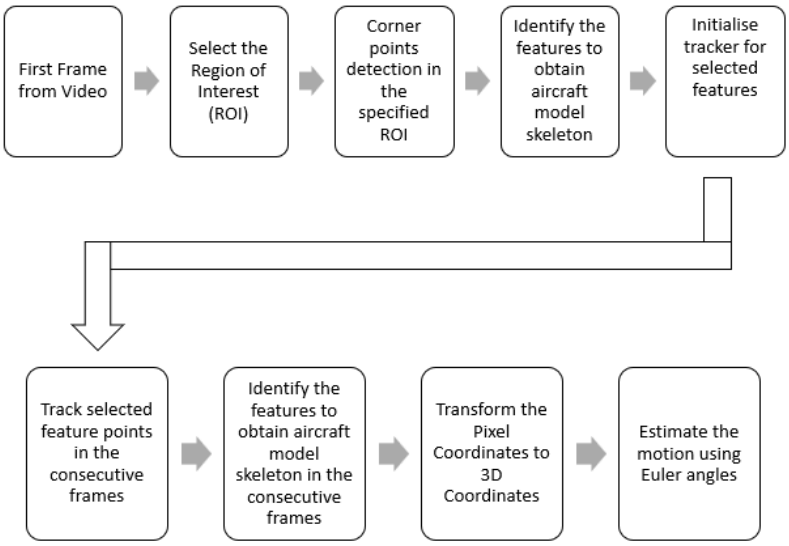

Fig. 3 Flow chart showing the process for motion estimation.

A. Features Detection

Harris corner and edge detection [23] is a well-known standard method for detecting features. It is used in the third stage of the process to detect the corner points of the aircraft image and is briefly summarized here.

Consider a 2D grey-scale image, F. An image window $W \in F$ is taken and is shifted by horizontal and vertical distances Δx and Δy respectively. The sum of squared differences S_W between values of the image F given in the

window W and its shifted variation by $\Delta x, \Delta y$ is given by:

$$S_W(\Delta x, \Delta y) = \sum_{x_i \in W} \sum_{y_j \in W} \left(F(x_i, y_j) - F(x_i - \Delta x, y_j - \Delta y)\right)^2. \tag{1}$$

If the shifted image window is approximated using a first-order Taylor's expansion, then the minimum of $S_W(\Delta x, \Delta y)$ is obtained analytically as

$$S_W(\Delta x, \Delta y) = \sum_{x_i \in W} \sum_{y_j \in W} \begin{bmatrix} \Delta x & \Delta y \end{bmatrix} \left(\begin{bmatrix} \frac{\partial F}{\partial x} \\ \frac{\partial F}{\partial y} \end{bmatrix} \begin{bmatrix} \frac{\partial F}{\partial x} & \frac{\partial F}{\partial y} \end{bmatrix} \right) \begin{bmatrix} \Delta x \\ \Delta y \end{bmatrix}, \tag{2}$$

and the Harris matrix $M_W(\Delta x, \Delta y)$ is the second derivative of S_W around the point $(\Delta x, \Delta y) = (0, 0)$ given by

$$M_W(\Delta x, \Delta y) = \begin{bmatrix} A & C \\ C & B \end{bmatrix}, \tag{3}$$

where

$$A = \sum_{x_i \in W} \sum_{y_j \in W} \frac{\partial^2 F(x_i, y_j)}{\partial x^2}, \tag{4}$$

$$B = \sum_{x_i \in W} \sum_{y_j \in W} \frac{\partial^2 F(x_i, y_j)}{\partial y^2}, \tag{5}$$

$$C = \sum_{x_i \in W} \sum_{y_j \in W} \frac{\partial F(x_i, y_j)}{\partial x} \frac{\partial F(x_i, y_j)}{\partial y} \tag{6}$$

Let λ_1, λ_2 be the eigenvalues of the matrix M_W, which is real and symmetric giving positive real eigenvalues. Hence we obtain three distinct cases as follows.

1) Both eigenvalues are small. This means that image F is flat at the examined pixel. There are no edges or corners in this location.
2) One eigenvalue is small and the other is large. The local neighborhood is ridge-shaped. Significant change of image F occurs if small movement is made perpendicularly to the ridge. This means that image F has an edge at the examined pixel.
3) Both eigenvalues are large. A small shift in any direction causes significant change of image F. This means that image F has a corner at the examined pixel.

To evaluate the cases and determine the existence of an edge or corner requires a measure of the corner and edge quality (response) along with a classification method. The response function, r_F, is given by

$$r_F = \det(M) - k \operatorname{tr}(M)^2 \tag{7}$$

where, $\det(M)$ denotes the determinant of M, $\operatorname{tr}(M)$ the trace of M, and k is tunable parameter. The response function classification is shown in Figure 4 [23]. The contours of the response function are shown by the fine line curves.

To apply to the images of the aircraft, Region of Interest (ROI) for fuselage length and wing span are selected and the corner points are obtained in these ROIs using the MATLAB Computer Vision Toolbox `detectHarrisFeatures` routine.

B. Feature Tracking

The Kanade-Lucas-Tomasi method [24, 25] is used to track the initialized corner points from subsection III.A for the feature point tracking stage shown in Figure 3. An outline of the method is given here.

The first image acquired at time t is defined by intensity function $I(x, y, t)$ and the second image acquired at the time $t + \tau$ as

$$I(x, y, t + \tau) = I(x - \Delta x, y - \Delta y, t). \tag{8}$$

The main objective of the tracking is to calculate the displacement (D) of the point $P = (x, y)$ between time instants t and $t + \tau$ which is defined as $D = \Delta x, \Delta y$. Small windows are used to estimate the displacement vector parameters.

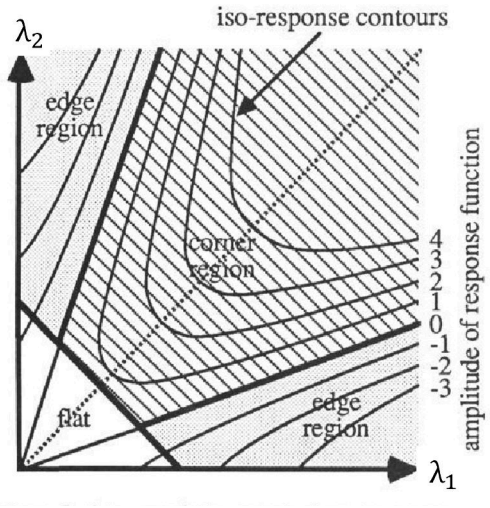

Fig. 4 Response function contours [23].

Any discrepancy between successive windows that cannot be explained by a translation is considered to be error, and the displacement vector is chosen to minimize this residual error.

Denoting $J(P) = I(x, y, t+\tau)$ and $I(P-D) = I(x-\Delta x, y-\Delta y, t)$ we have

$$J(P) = I(P-D) + n(P), \tag{9}$$

where n is noise. A double integral over the given window defines the displacement vector chosen to minimize the residue error so that

$$\epsilon = \iint_W [I(P-D) - J(P)]^2 \xi dP, \tag{10}$$

where W is the window, and ξ is a weighting function which can be set to unity or can be a Gaussian function. When the displacement in small, the intensity function can be approximated by its Taylor series in linear term,

$$I(P-D) = I(P) - g \cdot D. \tag{11}$$

The residual is defined as

$$\epsilon = \iint_W [I(P) - g \cdot D - J(P)]^2 \xi dP, \tag{12}$$

$$= \iint_W (h - g \cdot D)^2 \xi dP, \tag{13}$$

where $h = I(P) - J(P)$. This residual is a quadratic function of the displacement D. As a consequence, the minimisation can be done in closed form. Differentiating the residual (13) with respect to D and obtaining the turning points gives

$$\iint_W (h - g \cdot D)\, g \xi dA = 0. \tag{14}$$

Since $(g \cdot D)\, g = \left(gg^T\right) D$ and D is assumed constant within W, we have

$$\left(\iint_W gg^T \xi dA\right) D = \iint_W hg\xi dA. \tag{15}$$

Since it is a system of two scalar equation in two unknowns, it can be rewritten as $GD = E$ where the coefficient matrix is symmetric and is given by

$$G = \iint_W gg^T \xi dA, \tag{16}$$

and the right hand-side is

$$E = \iint_W (I - J) g \xi dA. \tag{17}$$

For every pair of adjacent frames, the matrix G can be computed from one frame by estimating gradients and computing their second order moments. The vector E on the other hand can be computed from the difference between the two frames, along with the gradient computed above.

C. Camera Parameters

1. Transformation from 2D to 3D

The problem is to detect the position of the corner points in a 3D space from its image point which is a projection of the 3D point onto the plane. This is depicted in Figure 5. The transformation is described here and is the penultimate stage of the process shown in Figure 3.

Transforming a corner point on a 2D plane, identified in subsections III.A and III.B,to a 3D point is performed by the following method. The pixel coordinates (u, v) obtained from an image are transformed to image coordinates by

$$X_I = d_{px}(u - c_x), \tag{18}$$
$$Y_I = d_{py}(v - c_y), \tag{19}$$

where, c_x, c_y is the principal point and (d_{px}, d_{py}) is the metres/pixel scaling pair. Since all the points lie on the image plane, the camera coordinates are obtained by,

$$\begin{bmatrix} X_c \\ Y_c \\ Z_c \end{bmatrix} = \begin{bmatrix} X_I \\ Y_I \\ f \end{bmatrix}. \tag{20}$$

The camera coordinates are transformed to 3D coordinates by

$$\begin{bmatrix} X \\ Y \\ Z \\ 1 \end{bmatrix} = \begin{bmatrix} R_c^T & t_c^T \end{bmatrix} \begin{bmatrix} X_c \\ Y_c \\ Z_c \end{bmatrix}. \tag{21}$$

where R_c is a rotation matrix of body coordinates to camera coordinates, t_c is a translation vector, and $(\cdot)^T$ denotes the transpose.

2. Transformation from 3D to 2D

The extrinsic parameters of rotation and translation are multiplied with a 3D point to obtain the point in the camera coordinate system by

$$\begin{bmatrix} X_c \\ Y_c \\ Z_c \end{bmatrix} = \begin{bmatrix} R_c & t_c \end{bmatrix} \begin{bmatrix} X \\ Y \\ Z \\ 1 \end{bmatrix}. \tag{22}$$

Multiplying this with the camera intrinsic parameters of focal length, f, and principal point, c_x, c_y, we obtain the 3D point in pixel coordinates given by

$$\begin{bmatrix} u' \\ v' \\ w' \end{bmatrix} = \begin{bmatrix} f & 0 & c_x \\ 0 & f & c_y \\ 0 & 0 & 1 \end{bmatrix} \begin{bmatrix} X_c \\ Y_c \\ Z_c \end{bmatrix}. \tag{23}$$

The 2D pixel coordinates are then obtained by

$$u = \frac{u'}{w'}, \quad v = \frac{v'}{w'}. \tag{24}$$

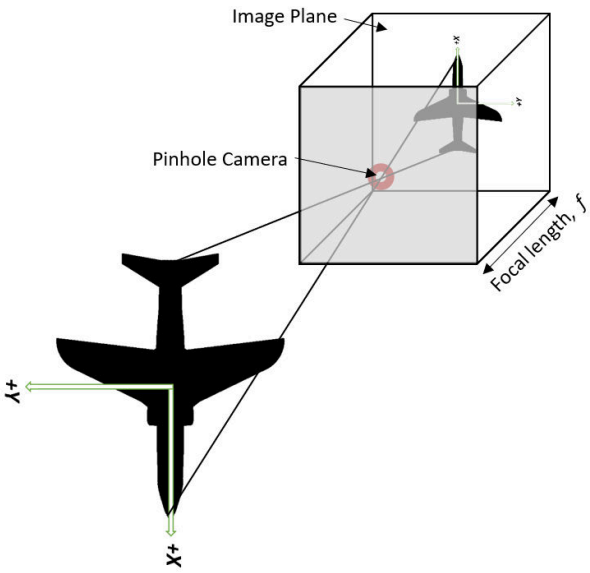

Fig. 5 Pinhole Camera.

3. Extrinsic Parameters of the Simscape Model

The rotation matrix, R_T, of body coordinates (X_b, Y_b, Z_b) to camera coordinates (X_c, Y_c, Z_c) in Simscape for a top view is given by

$$R_T = \begin{bmatrix} 1 & 0 & 0 \\ 0 & 1 & 0 \\ 0 & 0 & 1 \end{bmatrix}. \tag{25}$$

Similarly, the rotation matrix, R_S, of body coordinates to camera coordinates in Simscape for a side view is

$$R_S = \begin{bmatrix} 1 & 0 & 0 \\ 0 & 0 & 1 \\ 0 & -1 & 0 \end{bmatrix}. \tag{26}$$

The translation matrices for both the views are,

$$t_T = \begin{bmatrix} 0 & 0 & -50 \end{bmatrix}. \tag{27}$$

$$t_S = \begin{bmatrix} 0 & 50 & 0 \end{bmatrix}. \tag{28}$$

D. Camera Pose Estimation and Triangulation

In case the cameras were uncalibrated, the identified 2D points as described in section III.A and section III.B, their corresponding 3D points as described in section III.C.1 and the camera intrinsic parameters as described in section III.C.2 are utilized to estimate the essential matrix using the MATLAB Computer Vision Toolbox function `estimateEssentialMatrix`, and thereby estimate the relative pose of the side camera respect to the top camera using the function `estrelpose`. The function `estimateEssentialMatrix` is based on [26], [27] and [28].

This method of estimating relative pose of the camera, camera projection matrices of both the cameras induces error in position of the side camera. Since, the extrinsic parameters of both the cameras are known, relative pose of the side camera to the top camera can also be estimated by,

$$R_R = R_T' R_S \tag{29}$$

$$t_R = t_S - t_T \tag{30}$$

Using the above known parameters and triangulating 3D points using the function `triangulate` based on Direct Linear Transformation [19] also induces errors in identifying the corresponding 3D points due to the limitation of sensitivity to noise.

E. Aircraft Model Skeleton

Since the above triangulation method is error prone, an alternative is proposed here. Corner points of the aircraft namely the nose tip, midpoint of the horizontal stabilizer (HS), and wing tips are identified from the top view camera. The wing tips are transformed from 2D pixel points to 3D points using the top view camera parameters, and transformed from 3D to 2D using the side view camera parameters. This is done to identify the wing tips in the side view.

The corner points representing the nose tip, vertical stabilizer tip and midpoint of the horizontal stabilizer are identified from the side view camera. The vertical stabilizer tips are mapped to the camera's top view in a similar manner as the wing tips. The corner points from both camera views are integrated together to obtain the whole aircraft skeleton, as is shown in Figure 6.

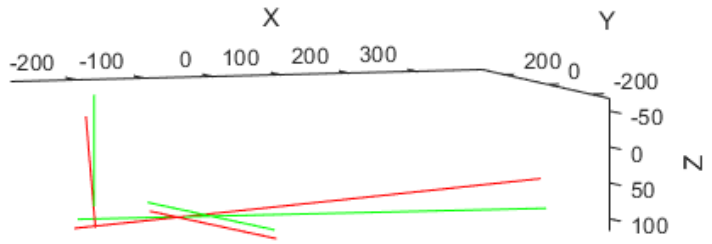

Fig. 6 Aircraft skeleton in 3D.

F. Euler Angles

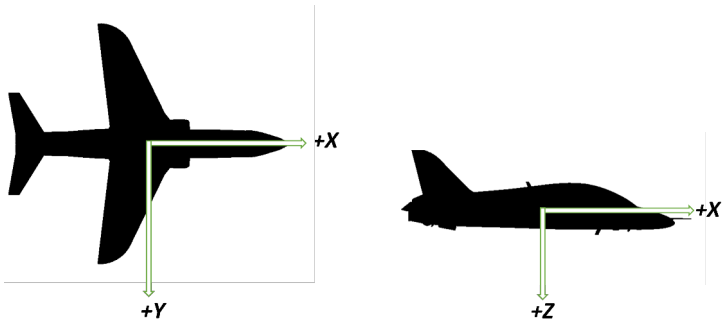

Fig. 7 Aircraft Model Axes

The final stage of the process shown in Figure 3 is to extract the Euler Tait-Bryan angles (roll, pitch, yaw). The aircraft model is given the standard body axes used for aircraft dynamics which are depicted in Figure 7. The rotation matrices for roll pitch and yaw are given next. The rotation matrix for a roll rotation around the X-axis through the angle ϕ is given by,

$$R_X = \begin{bmatrix} 1 & 0 & 0 \\ 0 & \cos\phi & \sin\phi \\ 0 & -\sin\phi & \cos\phi \end{bmatrix}. \tag{31}$$

The rotation matrix around the new Y-axis is a pitch rotation through the angle θ and is given by,

$$R_Y = \begin{bmatrix} \cos\theta & 0 & -\sin\theta \\ 0 & 1 & 0 \\ \sin\theta & 0 & \cos\theta \end{bmatrix}. \tag{32}$$

The final rotation is around the Earth frame Z-axis through a yawn angle ψ with a rotation matrix

$$R_Z = \begin{bmatrix} \cos\psi & \sin\psi & 0 \\ -\sin\psi & cos\psi & 0 \\ 0 & 0 & 1 \end{bmatrix}. \tag{33}$$

Multiplying the rotation matrices to obtain the Euler angle rotation matrix (known as the Direction Cosine Matrix),

$$R = R_X R_Y R_Z, \tag{34}$$

giving

$$R = \begin{bmatrix} \cos\theta\ \cos\psi & \cos\theta\ \sin\psi & -\sin\theta \\ \sin\phi\ \sin\theta\ \cos\psi - \cos\phi\ \sin\psi & \sin\phi\ \sin\theta\ \sin\psi + \cos\phi\ \cos\psi & \sin\phi\ \cos\theta \\ \cos\phi\ \sin\theta\ \cos\psi + \sin\phi\ \sin\psi & \cos\phi\ \sin\theta\ \sin\psi - \sin\phi\ \cos\psi & \cos\phi\ \cos\theta \end{bmatrix} \tag{35}$$

The Euler angles can be extracted from the DCM, (R) and are given by

$$\theta = \arctan\left(\frac{-R_{13}}{\sqrt{R_{11}^2 + R_{12}^2}}\right), \tag{36}$$

$$\psi = \arctan\left(\frac{R_{12}}{R_{11}}\right), \tag{37}$$

$$\phi = \arctan\left(\frac{R_{23}}{R_{33}}\right). \tag{38}$$

The Euler rate ($\dot{\phi}$) is obtained by backward difference numerical differentiation as follows,

$$\dot{\phi} = \frac{\phi(t) - \phi(t-1)}{\Delta t}. \tag{39}$$

Although this method causes a time shift, it is the feasible solution for implementation in a real-time system. The angular rates $\dot{\theta}$ and $\dot{\psi}$ are similarly obtained.

1. Euler Angles from Aircraft Skeleton

The DCM (R) from equation (35) is obtained from the 6 corner points of the aircraft skeleton obtained from section III.E by,

$$R = P_f {P_i}^{\dagger} \tag{40}$$

where, P_f and P_i are the matrices of the corner points of the final frame and the initial frame respectively, ${P_i}^{\dagger}$ is the pseudo-inverse of P_i. The Euler angles are obtained from the DCM using the equations (36), (37), (38).

G. 3D CAD Simulation

A 3D CAD model of a 1/12 scaled BAe Hawk is designed in SolidWorks. This model is imported to MATLAB Simscape to model and simulate the aircraft's motion. A Simscape model is designed with gimbal joints to enable Euler angle transformation of the CAD model and a transform sensor to obtain the rotation matrix.

The angles ϕ, θ and ψ are applied to the Simscape model estimated from the rotation matrix. For this paper, just a single degree-of-freedom experiment is presented. The pitch angle is varied sinusoidally while the roll and yaw are fixed at zero. Figures 8 and 9 show the applied pitch angle and rate. Note that there is numerical rounding noise on the roll and yaw angles.

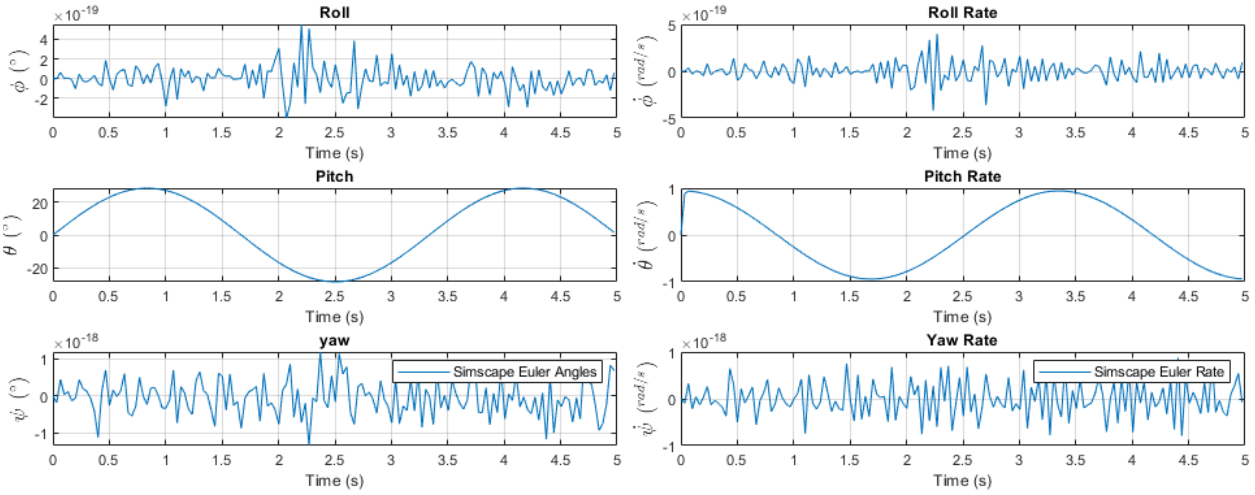

Fig. 8 Simscape Euler angles

Fig. 9 Simscape Euler rates.

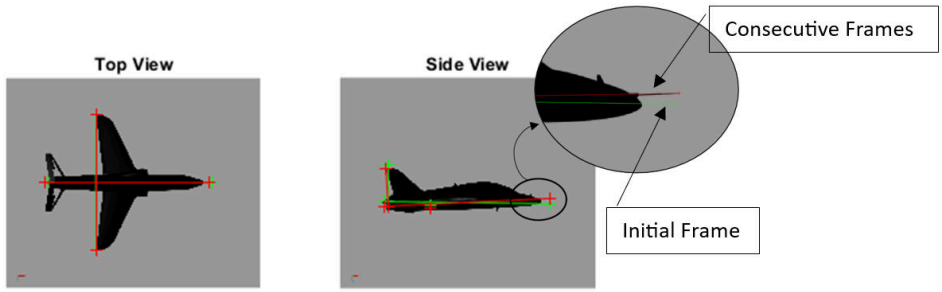

Fig. 10 Initial Frame and Consecutive Frame.

H. Sensitivity Analysis

The Euler angles equations obtained from the DCM (40) can be written as follows,

$$\phi = \arctan\left(\frac{\sum_{n=1}^{6} Y_{f,n} P^{\dagger}_{i\,(n,3)}}{\sum_{n=1}^{6} Z_{f,n} P^{\dagger}_{i\,(n,3)}}\right) \tag{41}$$

$$\theta = \arctan\frac{-\left(\sum_{n=1}^{6} X_{f,n} P^{\dagger}_{i\,(n,3)}\right)}{\sqrt{\left(\sum_{n=1}^{6} Y_{f,n} P^{\dagger}_{i\,(n,3)}\right)^2 + \left(\sum_{n=1}^{6} Z_{f,n} P^{\dagger}_{i\,(n,3)}\right)^2}} \tag{42}$$

$$\psi = \arctan\left(\frac{\sum_{n=1}^{6} X_{f,n} P^{\dagger}_{i\,(n,2)}}{\sum_{n=1}^{6} X_{f,n} P^{\dagger}_{i\,(n,1)}}\right) \tag{43}$$

where, n is the number of corner points of aircraft skeleton. The first-order Taylor series is used to perform sensitivity analysis of the method as it is a powerful tool for approximating the change in a function due to small perturbations in its input variables. The functions can be written as,

$$\phi(P_f + \delta P_f, P_i + \delta P_i) \approx \phi(P_f, P_i) + \frac{\partial \phi}{\partial P_f}\delta P_f + \frac{\partial \phi}{\partial P_i}\delta P_i \tag{44}$$

$$\theta(P_f + \delta P_f, P_i + \delta P_i) \approx \theta(P_f, P_i) + \frac{\partial \theta}{\partial P_f}\delta P_f + \frac{\partial \theta}{\partial P_i}\delta P_i \tag{45}$$

$$\psi(P_f + \delta P_f, P_i + \delta P_i) \approx \psi(P_f, P_i) + \frac{\partial \psi}{\partial P_f}\delta P_f + \frac{\partial \psi}{\partial P_i}\delta P_i \tag{46}$$

The equations of Euler angles (41), (42), and (43) have Moore-Penrose pseudo-inverse terms and the derivative of the matrix is given in [29] and can be modified for (${P_i}^\dagger$) as,

$$\mathrm{d}{P_i}^\dagger = -{P_i}^\dagger \, \mathrm{d}P_i \, {P_i}^\dagger + {P_i}^\dagger \, {{P_i}^\dagger}^T \, \mathrm{d}{P_i}^T \left(I - P_i {P_i}^\dagger\right) + \left(I - {P_i}^\dagger P_i\right) \mathrm{d}{P_i}^T \, {{P_i}^\dagger}^T \, {P_i}^\dagger \tag{47}$$

Sensitivity analysis of the method is conducted by computing the Jacobian matrices $\frac{\partial \phi}{\partial P_f}$, $\frac{\partial \theta}{\partial P_f}$, $\frac{\partial \psi}{\partial P_f}$, $\frac{\partial \phi}{\partial P_i}$, $\frac{\partial \theta}{\partial P_i}$ and $\frac{\partial \psi}{\partial P_i}$ with respect to each of the 6 initial and final frame world coordinates (X, Y, Z) of the aircraft skeleton.

IV. RESULTS

The intermediate results of the identification of the aircraft skeleton from the side and top images are discussed first. This is because the motion estimation is highly sensitive to the position of the corner points of aircraft model skeleton.

Identifying the corner points using Harris corner detection results in a varying error in the pixel coordinates (u, v) which causes an error in estimation of Euler angles. The errors from the Harris detection for just a single frame example are given in table 1. Figure 10 illustrates the corner points and aircraft model skeleton in pixel coordinates, where green and red colours represents the initial frame and a consecutive frame respectively.

Corner points	X pixel error	Y pixel error
Top View HS	2.052	±1.052
Side View HS P1	1.229	-1.171
Side View HS P2	1.257	-1.047
Top View Wing P1	2.052	0.052
Top View Wing P2	1.060	0.583
Side View Tail P1	0.880	1.312

Table 1 Harris detection method errors.

	Angles Error (°)		Rates Error (rad/s)
ϕ	[-0.0611, +0.0915]	$\dot{\phi}$	[-0.0036, +0.0034]
θ	[-3.2346, +1.0573]	$\dot{\theta}$	[-0.1134, +0.1117]
ψ	[-0.0336, 0]	$\dot{\psi}$	[-0.0118, +0.0043]

Table 2 Error range of the proposed method.

A transformation of 2D pixel coordinates to 3D coordinates of aircraft model skeleton as described in subsection III.E is illustrated in Figure 6. Figures 11 and 12 compare the Euler angles and Euler rates from our proposed vision method and Simscape data respectively. Furthermore, these figures visually demonstrate the range of variation, while table 2 provides a comprehensive numerical representation of these error ranges. Overall, the ϕ, ψ angles and $\dot{\phi}, \dot{\psi}$ rates have relatively small errors and are unlikely to have significant impact on the flight dynamics model. However, θ angles and $\dot{\theta}$ rates have much larger errors and exhibit a consistent bias towards underestimation and have significant impact on the flight dynamics. These errors follow a sine ave pattern because the input to the Simscape model is a sine wave.

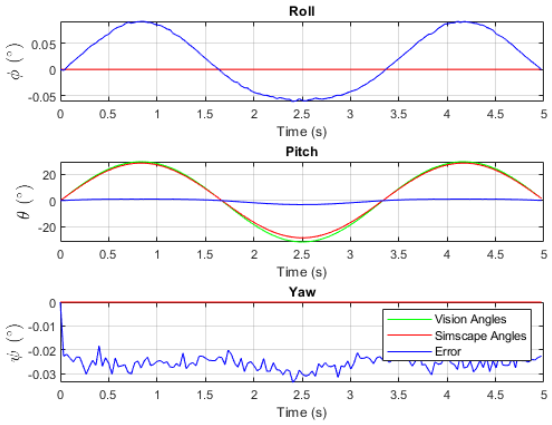

Fig. 11 Vision and Simscape Euler angles.

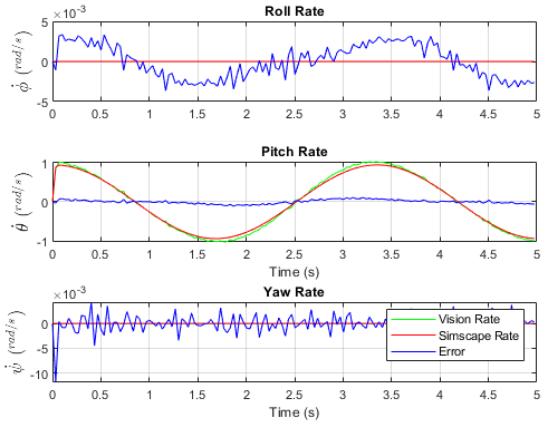

Fig. 12 Vision and Simscape Euler rates.

These errors are caused by various factors such as, errors in accurate identification of aircraft skeleton as mentioned in table 1, numerical instability due to P_i matrix inversion, and errors caused by approximation of the eigenvectors of P_i matrix for matrix inversion which amplifies the errors in P_i. Similarly, figures 13 and 14 compare the Euler angles from the DLT triangulation as described in section III.D to the Simscape data and table 3 details the error range. Alongside the previously mentioned sources of error of our proposed method, the DLT triangulation method itself is a primary cause of substantial inaccuracies in the determination of Euler angles here. Likewise, figures 15 and 16 compare the Euler angles from the DLT triangulation as described in section III.D to the our proposed method as described in III.E and table 4 details the error range between both the methods.

Table 5 lists the results of the sensitivity analysis described in III.H that is the change in Euler angles respective to a change in world coordinates by a randomised number between -1, +1. The magnitude of sensitivity coefficients of ϕ, ψ is relatively small which indicates that the change in these angles are small compared to the change in the P_f, P_i coordinates. The magnitude of sensitivity coefficients of θ is relatively larger which indicates that the change in θ is substantial compared to the change in P_f, P_i coordinates. Figures 17, 18 and 19 depict the sensitivity coefficients of functions ϕ, θ, and ψ with respect to the world coordinates.

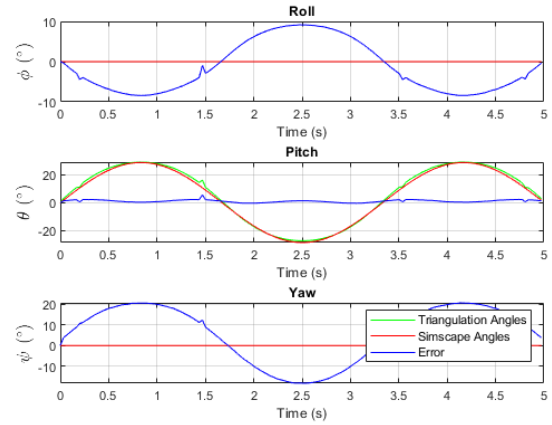

Fig. 13 DLT and Simscape Euler Angles.

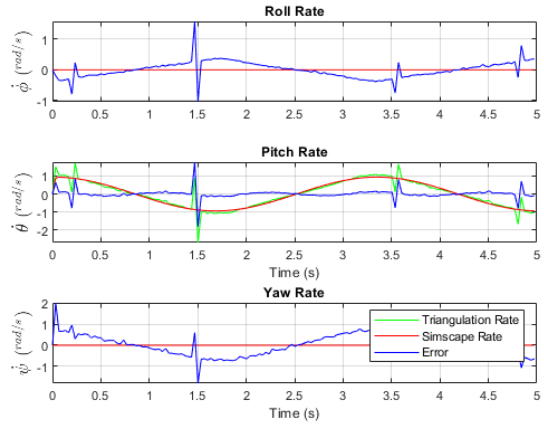

Fig. 14 DLT and Simscape Euler Rates.

	Angles Error (°)		Rates Error (rad/s)
ϕ	[-8.4232, +9.1544]	$\dot{\phi}$	[-1.0423, +1.5736]
θ	[-0.5285, +5.4768]	$\dot{\theta}$	[-1.8154, +1.7763]
ψ	[-18.3760, +20.7626]	$\dot{\psi}$	[-1.7981, +2.0070]

Table 3 Error range of triangulation method.

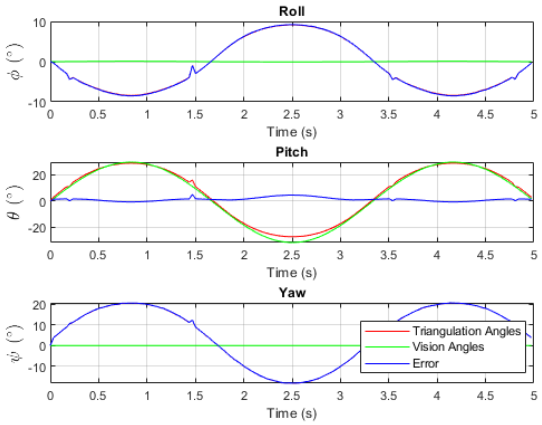

Fig. 15 DLT and Vision Euler Angles.

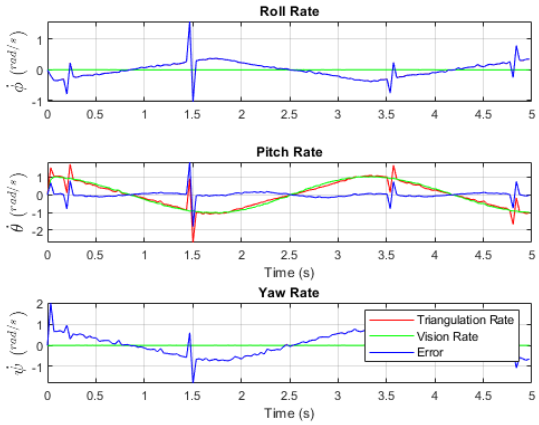

Fig. 16 DLT and Vision Euler Rates.

	Angles Error (°)		Rates Error (rad/s)
ϕ	[-8.5144, +9.2105]	$\dot{\phi}$	[-1.0395, +1.5765]
θ	[-0.7526, +4.9997]	$\dot{\theta}$	[-1.7896, +1.8408]
ψ	[-18.3458, +20.7843]	$\dot{\psi}$	[-1.7977, +2.0188]

Table 4 Error range between both the methods.

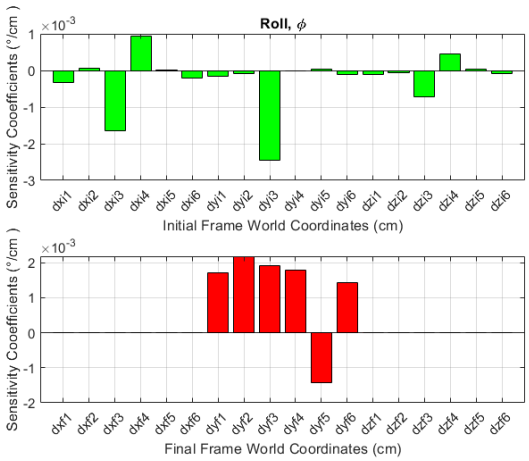

Fig. 17 DCM Roll Sensitivity

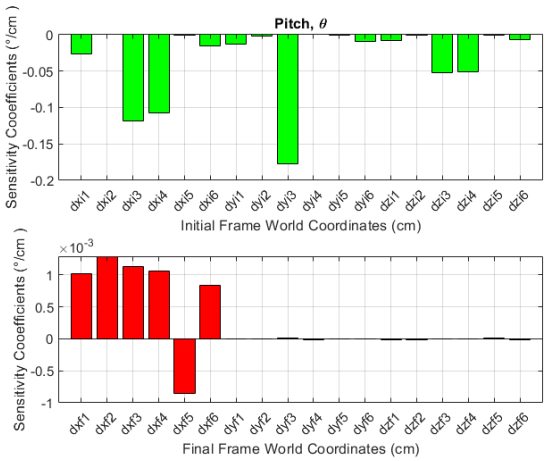

Fig. 18 DCM Pitch Sensitivity

Euler Angle	Euler Angle Change
ϕ	-0.0027°
θ	0.1547°
ψ	-0.0011°

Table 5 Sensitivity Analysis.

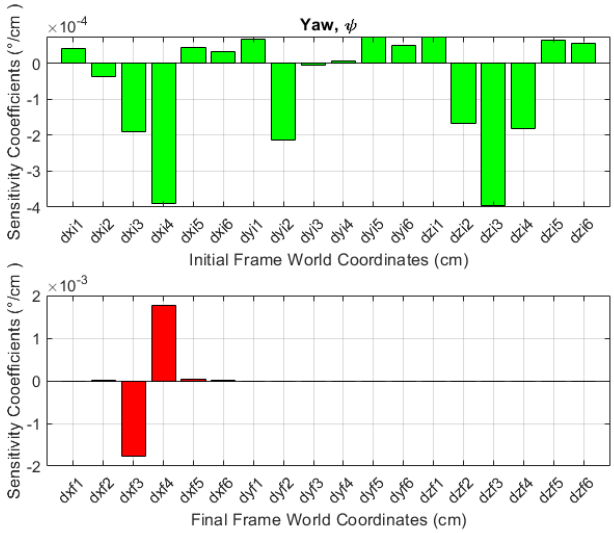

Fig. 19 DCM Yaw Sensitivity

V. CONCLUSION

A computer vision technique is proposed for motion estimation of scaled models in wind tunnel testing without having any markers on the model. This has not been implemented before. The technique proposed is a sequence of Harris corner detection, Kanade-Lucas-Tomasi tracking, and Euler angles. The Harris detection method gives errors in identifying the corner points of aircraft model skeleton and contributes errors in estimating Euler angles. Sensitivity analysis of the proposed method has been conducted by applying first-order Taylor series. Using DLT for triangulation of the 2D points contributes to the errors in Euler angles estimation which could be improved by performing a more accurate camera calibration.

Note that the developed method is not yet accurate enough for dynamic wind tunnel testing. Thus the approach requires improvement in order to be implemented for wind tunnel testing. The obvious way to improve the method is to place markers on the aircraft model. This, however, limits the wider applicability of the proposed approach, which could also be applied for vision systems in for example, air traffic management, or for determining hostile intent by enemy aircraft. For application to wind tunnel testing, the method can however be augmented by other measurements such as an IMU for estimating motion dynamics or by contact measurements in the form of potentiometers on the aircraft attachment gimbal. In further work, given the potential advantages of quaternions in representing rotations, their application in Euler angles estimation over matrices will be investigated to assess their effectiveness and accuracy. The algorithm will be validated through its application on a scaled-down model of the BAe Hawk aircraft in a wind tunnel, along with the incorporation of other measurement techniques.

References

[1] Pontillo, A., Yusuf, S., Lopez, G., Rennie, D., and Lone, M., "Investigating pitching moment stall through dynamic wind tunnel test," *Proceedings of the Institution of Mechanical Engineers, Part G: Journal of Aerospace Engineering*, Vol. 234, No. 2, 2020, pp. 267–279. https://doi.org/10.1177/0954410019861853.

[2] Rajamurthy, M. S., "Generation of Comprehensive Longitudinal Aerodynamic Data Using Dynamic Wind-Tunnel Simulation,"

Journal of Aircraft, Vol. 34, No. 1, 1997, pp. 29–33. https://doi.org/10.2514/2.2157.

[3] Tortora, P., Huang, M., and Wang, Z., "A Review of Wind Tunnel Based Virtual Flight Testing Techniques for Evaluation of Flight Control Systems," *International Journal of Aerospace Engineering*, Vol. 2015, No. 672423, 2015. https://doi.org//10.1155/2015/672423.

[4] Owens, B., Brandon, J., Croom, M., Fremaux, M., Heim, G., and Vicroy, D., "Overview of Dynamic Test Techniques for Flight Dynamics Research at NASA LaRC," *25th AIAA Aerodynamic Measurement Technology and Ground Testing Conference*, 2012. https://doi.org/10.2514/6.2006-3146.

[5] Carnduff, S. D., Erbsloeh, S. D., Cooke, A. K., and Cook, M. V., "Characterizing stability and control of subscale aircraft from wind-tunnel dynamic motion," *Journal of Aircraft*, Vol. 46, No. 1, 2009, pp. 137–147. https://doi.org/10.2514/1.36730.

[6] Pattinson, J., Lowenberg, M. H., and Goman, M. G., "Multi-degree-of-freedom wind-tunnel maneuver rig for dynamic simulation and aerodynamic model identification," *Journal of Aircraft*, Vol. 50, No. 2, 2013, pp. 551–566. https://doi.org/10.2514/1.C031924.

[7] Araujo-Estrada, S. A., Gong, Z., Lowenberg, M. H., Neild, S., and Goman, M., "Wind Tunnel Manoeuvre Rig: A Multi-DOF Test Platform for Model Aircraft," *54th AIAA Aerospace Sciences Meeting*, 2016. https://doi.org/10.2514/6.2016-2119.

[8] Navaratna, P. D. B., Lowenberg, M. H., and Neild, S. A., "Minimally Constrained Flight Simulation in Wind Tunnel," *Journal of Aircraft*, Vol. 56, No. 4, 2019, pp. 1353–1366. https://doi.org/10.2514/1.C035199.

[9] Honeywell International Inc, "Honeywell Aerospace," `https://aerospace.honeywell.com/us/en/products-and-services/product/hardware-and-sys tems/sensors/inertial-measurement-units`, 2023. Accessed: 21 July 2023.

[10] Narasimhappa, M., Mahindrakar, A. D., Guizilini, V. C., Terra, M. H., and Sabat, S. L., "MEMS-Based IMU Drift Minimization: Sage-Husa Adaptive Robust Kalman Filtering," *IEEE Sensors Journal*, Vol. 20, No. 1, 2020, pp. 250–260. https://doi.org/10.1109/JSEN.2019.2941273.

[11] Chen, H., Aggarwal, P., Taha, T. M., and Chodavarapu, V. P., "Improving Inertial Sensor by Reducing Errors using Deep Learning Methodology," *IEEE National Aerospace and Electronics Conference (NAECON 2018)*, 2018, pp. 197–202. https://doi.org/10.1109/NAECON.2018.8556718.

[12] Chen, C., Lu, C. X., Wahlstrom, J., Markham, A., and Trigoni, N., "Deep Neural Network Based Inertial Odometry Using Low-Cost Inertial Measurement Units," *IEEE Transactions on Mobile Computing*, Vol. 20, No. 4, 2021, pp. 1351–1364. https://doi.org/10.1109/TMC.2019.2960780.

[13] Liu, W., Ma, X., Li, X., Chen, L., Zhang, Y., Li, X., Shang, Z., and Jia, Z., "High-precision pose measurement method in wind tunnels based on laser-aided vision technology," *Chinese Journal of Aeronautics*, Vol. 28, No. 4, 2015, pp. 1121–1130. https://doi.org/10.1016/j.cja.2015.05.009.

[14] Li, Z., Yang, M., Huang, S., and Zhou, D., "A new moving model test method for the measurement of aerodynamic drag coefficient of high-speed trains based on machine vision," *Proceedings of the Institution of Mechanical Engineers, Part F: Journal of Rail and Rapid Transit*, Vol. 232, No. 5, 2018, pp. 1425–1436. https://doi.org/10.1177/0954409717731233.

[15] Wu, L.-J., Casciati, F., and Casciati, S., "Dynamic testing of a laboratory model via vision-based sensing," *Engineering Structures*, Vol. 60, 2014, pp. 113–125. https://doi.org/https://doi.org/10.1016/j.engstruct.2013.12.002.

[16] Ha, J., Johnson, E. N., and Tannenbaum, A., "Real-Time Visual Tracking Using Geometric Active Contours and Particle Filters," *Journal of Aerospace Computing, Information, and Communication*, Vol. 5, No. 10, 2008, pp. 361–379. https://doi.org/10.2514/1.35527.

[17] Yoo, S., Kim, W., and Kim, C., "Saliency Combined Particle Filtering for Aircraft Tracking," *Journal of Signal Processing Systems*, Vol. 76, No. 1, 2014, p. 19–31. https://doi.org/10.1007/s11265-013-0803-x.

[18] Zheng, M., Wu, Z., Bakhdavlatov, S., Qu, J., Li, H., and Yuan, J., "Real-time aerial targets detection algorithm based background subtraction," *2013 Asia-Pacific Signal and Information Processing Association Annual Summit and Conference*, 2013, pp. 1–6. https://doi.org/10.1109/APSIPA.2013.6694203.

[19] Hartley, R., and Zisserman, A., *Multiple View Geometry in Computer Vision*, Cambridge University Press, Cambridge, U.K., 2003.

[20] Fischler, M. A., and Bolles, R. C., "Random Sample Consensus: A Paradigm for Model Fitting with Applications to Image Analysis and Automated Cartography," *Communications of the ACM*, Vol. 24, No. 6, 1981, p. 381–395. https://doi.org/10.1145/358669.358692.

[21] Lepetit, V., Moreno-Noguer, F., and Fua, P., "EPnP: An Accurate $O(n)$ Solution to the PnP Problem," *International Journal of Computer Vision*, Vol. 81, 2009, pp. 155–166.

[22] Gurfil, P., and Rotstein, H., "Computer vision-based estimation of aircraft dynamics," *Proceedings of the 40th IEEE Conference on Decision and Control*, 2001, pp. 3746–3751. https://doi.org/10.1109/CDC.2001.980446.

[23] Harris, C., and Stephens, M., "A Combined Corner and Edge Detector," *Proceedings of the Alvey Vision Conference*, Alvety Vision Club, 1988, pp. 23.1–23.6. https://doi.org/d10.5244/C.2.23.

[24] Tomasi, C., and Kanade, T., "Detection and Tracking of Point Features," Tech. Rep. CMU-CS-91-132, Carnegie Mellon University, 1991.

[25] Shi, J., and Tomasi, C., "Good features to track," *IEEE Conference on Computer Vision and Pattern Recognition*, 1994, pp. 593–600. https://doi.org/10.1109/CVPR.1994.323794.

[26] Kukelova, Z., Bujnak, M., and Pajdla, T., "Polynomial Eigenvalue Solutions to the 5-pt and 6-pt Relative Pose Problems," *British Machine Vision Conference*, 2008.

[27] Nister, D., "An efficient solution to the five-point relative pose problem," *IEEE Transactions on Pattern Analysis and Machine Intelligence*, Vol. 26, No. 6, 2004, pp. 756–770. https://doi.org/10.1109/TPAMI.2004.17.

[28] Torr, P. H. S., and Zisserman, A., "MLESAC: A New Robust Estimator with Application to Estimating Image Geometry," *Computer Vision Image Understanding*, Vol. 78, 2000, pp. 138–156.

[29] Golub, G., and Pereyra, V., "The Differentiation of Pseudo-Inverses and Nonlinear Least Squares Problems Whose Variables Separate," *SIAM Journal on Numerical Analysis*, Vol. 10, 1973, pp. 413–432. https://doi.org/10.1137/0710036.

2024-01-04

Motion estimation of an aircraft model using computer vision

Kasula, Pavithra

AIAA

Kasula P, Whidborne J, Rana ZA, Ishola A. (2024) Motion estimation of an aircraft model using computer vision. In: AIAA SCITECH 2024 Forum 2024, 8-12 January 2024, Orlando, USA
https://doi.org/10.2514/6.2024-2501